

Article

On-line Writing of Fiber Bragg Grating Array on a Two-mode Optical Fiber for Sensing Applications

Haihu Yu ¹, Wenjing Gao ¹, Xin Jiang ¹, Huiyong Guo ¹, Shan Jiang ² and Yu Zheng ^{1,*} 

¹ National Engineering Laboratory for Fiber Optic Sensing Technology, Wuhan University of Technology, Wuhan 430070, China; hhyu@whut.edu.cn (H.Y.); gaowenjing@whut.edu.cn (W.G.); jiangx@whut.edu.cn (X.J.); ghylucky@163.com (H.G.)

² Wuhan WUTOS Co., Ltd., Wuhan 430070, China; jiangshan@wutos.com

* Correspondence: zhengyu0816@whut.edu.cn; Tel.: +86-189-860-08488

Received: 22 March 2019; Accepted: 16 April 2019; Published: 17 April 2019



Abstract: On-line fabricated fiber Bragg grating (FBG) array and its sensing potentials have attracted plenty of attention in recent years. In this paper, FBG arrays are written on-line on a two-mode fiber, and this two-mode fiber Bragg grating (TM-FBG) is further experimentally investigated for temperature and curvature sensing. The responses of this sensor were characterized by 11.2 pm/°C and -0.21 dB/m⁻¹ for temperature and curvature, respectively. Based on the measurements, a dual-parameter fiber sensing system was developed, which can realize the quasi-distributed, simultaneous detection of temperature and curvature, making it suitable for structural health monitoring or perimeter security.

Keywords: two-mode fiber; fiber Bragg grating; on-line grating writing; temperature sensing; curvature sensing

1. Introduction

Fiber Bragg grating (FBG), as an important fiber technology, possesses advantageous properties for fiber-based sensors such as high resistance to electromagnetic interference, enhanced sensitivity, compact size and desirable network extensions [1,2]. Various physical quantities such as temperature, stress, curvature and refractive index have been well studied, using FBG-based fiber sensing devices [3–5]. A typical FBG is applied on single-mode fibers (SMFs), inscribed with periodic Bragg grating structure, so as called a single-mode FBG. Single-mode FBG is widely used in the fiber sensing field, which has characteristics of low transmission loss and single mode propagation [6]. Not only limited to SMFs, grating structures, in principle, can be written on any fiber with a sensitive core, for instance, a few-mode fiber. A few-mode fiber supports a limited number of transverse modes [7]. It has been demonstrated that pressure, stress and curvature sensing can be realized individually using a few-mode fiber based sensing system [8–11]. If now we consider combining it with the FBG technology, a few-mode FBG, therefore, it can be expected to be used for multi-parameter measurements and comparatively reduced cross-sensitivity, as observed in single-mode FBG [12–15].

Recently, FBG arrays and distributed sensing networks are attracting broad interests in the field of optical fiber sensing, from both industry and academic. Long-distance, large-capacity FBG array on SMFs have been demonstrated, using a FBG on-line written system [16,17]. In principle, the same technology can be applied to few-mode fibers. Unfortunately, due to technical difficulties, it has not been demonstrated. On the other hand, due to low transmission loss, few-mode FBG can be considered for long-distance signal transmission and multi-point distributed measurements.

In this paper, using the on-line FBG writing technique, two-mode fiber Bragg gratings (TM-FBGs) and a TM-FBG array are successfully fabricated. We then use the TM-FBG for sensing studies. Temperature and curvature sensing are experimentally investigated. Furthermore, based on the TM-FBG

array, a dual-parameter fiber sensing system is developed, which can realize the quasi-distributed simultaneous detection of temperature and curvature. To make the system practical, the potential application of TM-FBG array is discussed.

2. The Principle of the Two-Mode FBG

Firstly, we checked the transmission properties of a two-mode fiber in theory. Transverse modes, supported by an optical fiber, are determined by the structural parameters of the fiber, as well as the operating wavelength. In a step-index fiber, the normalized cut-off frequency V_c is given by:

$$V_c = \frac{2\pi}{\lambda_0} a \sqrt{n_1^2 - n_2^2}, \quad (1)$$

where λ_0 is wavelength, a is core radius of the fiber, and n_1 and n_2 are the refractive indices of the core and cladding glasses. Several lowest order linearly polarized (LP) modes and their corresponding V_c are given in Table 1 [18].

Table 1. Several lowest order linear polarization (LP) modes and their corresponding cut-off frequency V_c .

Cut-off V_c	LP mode
<2.405	only LP ₀₁
2.405	LP ₁₁
3.823	LP ₀₂ , LP ₂₁
5.136	LP ₃₁

From Table 1, when the V_c is within 2.405 and 3.823, only the two LP₀₁ and LP₁₁ modes are supported. Based on Equation (1), the V_c , the core radius (a) and the difference of refractive index between the core and cladding materials (n_1 and n_2) can be adjusted. We then used the COSMOL Multiphysics to make the finite element method (FEM) calculations, in order to figure out the expected fiber parameters.

We first checked the standard SMF G.652. The refractive indices of the fiber core n_1 and cladding n_2 are set as 1.450 and 1.445; the initial fiber diameter $2r_2$ is 125 μm , and the core diameter $2r_1$ is 8.3 μm . The working wavelength is 1550 nm. The results are shown in Figure 1. When the fiber diameter increases from 125 μm to 240 μm , the core diameter ramps up from 8.3 μm to 15.9 μm gradually. The fiber starts to support the LP₀₁ and LP₁₁ modes, when its outer diameter is larger than 175 μm . The co-existence of the two modes is kept, when the fiber diameter is between 175 and 240 μm . The LP modes are superpositions of vector modes namely HE and TE/TM modes, for example, the LP₁₁ mode, is four-fold degeneracy of the HE₂₁, TE₀₁ and TM₀₁ modes, as clearly depicted in the results of the numerical simulations, as seen in Figure 1.

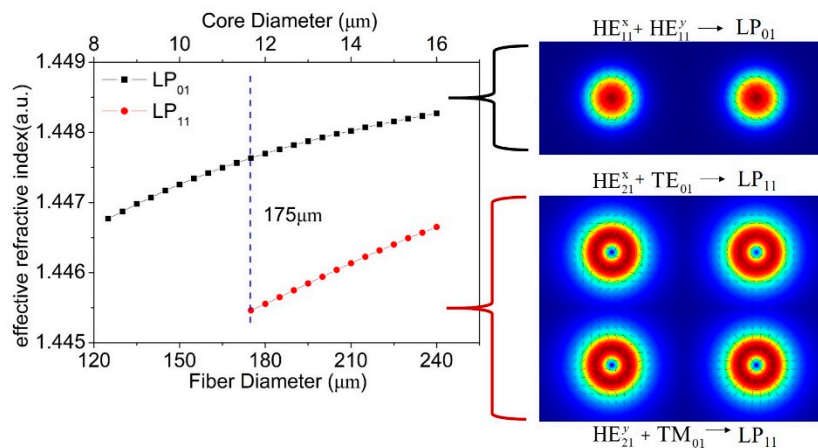


Figure 1. The relation between the transmission mode and diameter of the fiber the insets are mode fields of vector modes in two-mode fiber and the relationship of vector modes and LP modes.

Furthermore, we analyzed the characteristics of FBG in the two-mode fiber. Based on the coupled-mode theory of FBG, modes coupling happens between the forward and backward propagating core modes in FBG, when the absolute values of the propagation constants are identical. The reflection spectra of a single-mode FBG with a fiber outer diameter of 125 μm and a two-mode FBG with a fiber outer diameter of 200 μm were investigated. The grating period Λ was set at 535.59 nm, and the reflection spectra were calculated by transfer matrix method based on coupled-mode theory. The results are plotted in Figure 2. Figure 2a and c show the curve of the mode propagation constant and reflection spectrum of the single-mode FBG. According to the calculations (Figure 2a), the propagation constant of the LP_{01} mode decreases monotonically with the increase of wavelength, while the grating resonance is independent of the wavelength change. The propagation constant and the grating resonance have only one intersection (marked as A) at the wavelength of 1550.90 nm, corresponding to the central wavelength (marked as A') of FBG in the reflection spectrum, as shown in Figure 2c. Figure 2b shows the relationship of calculated propagation constants and resonance condition of the LP_{01} mode, LP_{11} mode and the coupled mode in two-mode fiber, of which the grating resonance wavelength are marked as B, C and D, corresponding to the three wavelength of TM-FBG in Figure 2d. Due to the co-existence of the LP_{01} and LP_{11} modes in the fiber, each mode has a specific wavelength satisfying the grating resonance condition, which are at wavelengths 1549.90 nm (B') and 1552.00 nm (D'), respectively. In addition, mode coupling exists between the two LP modes, which forms a coupled-mode [19]. This coupled-mode in TM-FBG is generated by the coupling between the forward mode of LP_{01} mode and the backward mode of LP_{11} mode or the forward mode of LP_{11} mode and the backward mode of LP_{01} mode. The propagation constant of the coupled mode is approximately one half of the sum, of those the two LP modes. The resonance wavelength of the coupled mode is at around 1550.95 nm (C'). Based on the above analysis, it is found that this TM-FBG has three characteristic reflections, and they are considered for later sensing experiments.

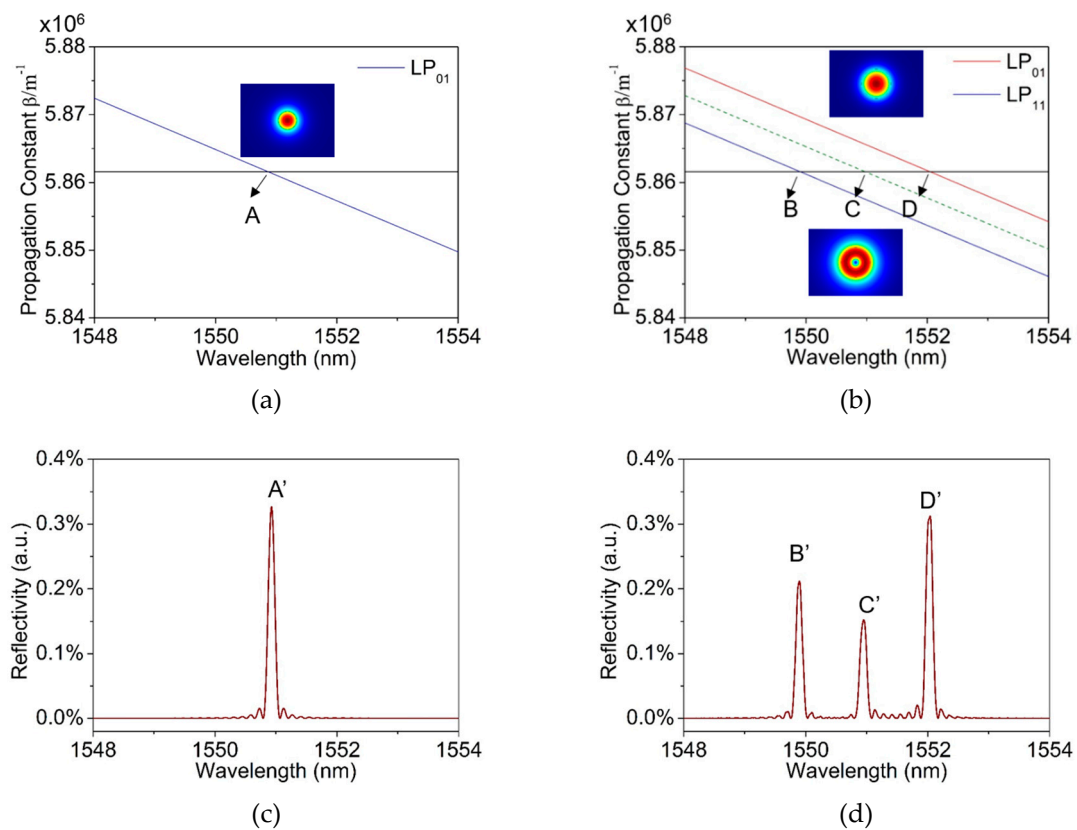


Figure 2. The formation mechanism of fiber Bragg grating (FBG) in a single-mode fiber and a two-mode fiber, the horizontal line (in black) refers to the propagation constant and the colorful curves depict the resonance condition. (a) The intersection refers A to FBG resonance condition in single-mode fiber, the inset plots the mode field of LP₀₁ mode; (b) the intersections, B, C and D, refer to resonance conditions for LP₀₁ mode, LP₁₁ mode and the coupled mode in two-mode fiber, the insets plot the mode fields of LP₀₁ and LP₁₁ modes; (c) reflection spectrum of the single-mode FBG; and (d) reflection spectrum of the two-mode FBG.

The first order high order mode (HOM) LP₁₁ is prone to fiber bending, as compared to the fundamental mode (FM) LP₀₁. Using COSMOL, the confinement loss is calculated by [20]:

$$\alpha_{loss} = 8.686 \times \frac{2\pi}{\lambda[\mu\text{m}]} \times \text{Im}(n_{eff}) \times 10^9 [\text{dB}/\text{km}] \quad (2)$$

where the $\text{Im}(n_{eff})$ is the imaginary part of the effective refractive index, of a supported mode. The confinement losses of the LP₀₁ and LP₁₁ modes, under the bending curvatures ranging from 35 m⁻¹ to 100 m⁻¹, were calculated (Figure 3). It can be seen that the confinement loss of the LP₀₁ mode (black dots) remained small ($\sim 10^{-4}$ dB/m), while the loss of the LP₁₁ mode (red dots) increased significantly from 0.25 to 0.6 dB/m, when the curvature ramped up from 35 m⁻¹ to 100 m⁻¹. The LP₁₁ mode is deemed as a leaky mode when fiber is bent. Due to this feature, by carefully identifying the reflection peak of the LP₁₁ mode, the TM-FBG can be possibly used for curvature sensing. In addition, by measuring the shift of the reflection wavelength of the LP₁₁ mode, temperature or strain sensing can also be realized simultaneously, using the same TM-FBG.

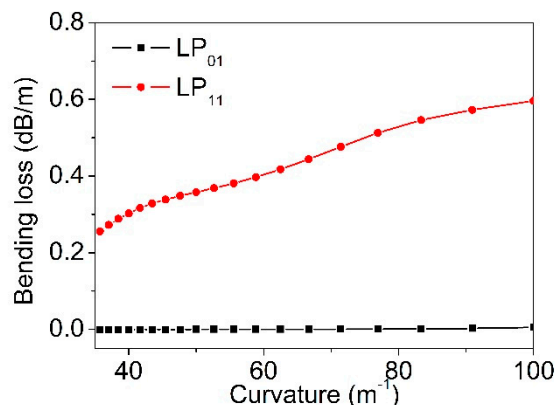


Figure 3. The simulation of two modes: Confinement loss when the curvature increases.

3. Online Writing of FBG Array

FBG arrays inscribed with various gratings can be written by using the on-line writing system on our customized drawing tower. Figure 4a shows the schematic diagram of the drawing tower, affiliated with the FBG on-line writing system. A fiber preform with a germanium-doped, photosensitive core is fed continuously into a graphite resistance furnace. After heated to over 1900 °C, the preform is to be drawn into bare fibers. With precise control of the parameters such as furnace temperature, drawing and feeding speed, fiber tension and preform position, the final fiber can be produced with expected dimensions. Before the fiber goes through a double-coating and UV curing unit, there is a FBG writing platform which FBG array can be written on the fiber. After being written, the fiber is then directed to the collection wheel on the ground floor. Using the on-line writing technique, a large number of FBGs can be continuously inscribed in a single fiber piece of a long distance (e.g., 50 km), without complex post-processing steps such as coating decortication, grating inscription and fiber-splicing, as required by conventional FBG writing. This technique brings advantages such as highly consistent grating reflectivity, increased mechanical strength and reduced splicing loss.

FBG arrays can be written in real time during fiber drawing. Figure 4b shows the FBG writing stage. An excimer laser operating at 193 nm wavelength acts as the UV irradiation source, of which the laser spot size is 6 mm × 12 mm. The pulse width is ~10 ns, and the maximum repetition rate is 500 Hz. The maximum available pulse energy is ~10 mJ. A phase mask is placed ~0.1 mm next to the bare fiber, with a mask size of 10 mm × 10 mm. The laser beam goes through three cylindrical lenses and is then focused onto the phase mask with beam line of 0.7 mm × 10 mm. Through the phase mask, ±1st interference fringes are generated and expose to the bare fiber to inscribe FBG. The period of grating Λ is determined by:

$$\Lambda = \frac{\Lambda_{\text{mask}}}{2}, \quad (3)$$

where Λ_{mask} is the period of the phase mask.

Based on this system, a two-mode FBG array was successfully written on a step-index fiber with a photosensitive core. The optical fiber preform for FBG inscription was the glass preform, with a low amount of germanium, less than 0.6%, doped in the fiber core and the numerical aperture (NA) of 0.14. The fiber possessed the same structure as the standard single-mode optical fiber G.652. The pitch of the phase mask was 1071.93 nm and the laser pulse energy was 8 mJ. The preform used for fiber drawing was a standard one for SMF with a fiber core diameter 8.3 μm , and we used the same preform for the fabrication of the two-mode (TM) fiber. Based on our theoretical calculations, it was found for a fiber to support two modes, the core diameter needs to be expanded to 13.3 μm , so as the fiber outer diameter to be ~200 μm . By controlling the preform feeding and fiber drawing rates, the diameter of fiber was increased from 125 μm to 200 μm , for the reason to draw a TM fiber. To avoid the occurrence of excessive shaking and breaking in grating fabrication process, the drawing speed was controlled at 10–15 m/min and the average drawing tension at 10–30 N. Experimental reflection spectra of the FBG

with the fiber diameter of 125 μm and 200 μm are shown respectively in Figure 5a,b, which are in good agreement with the theoretical plots in Figure 2c,d.

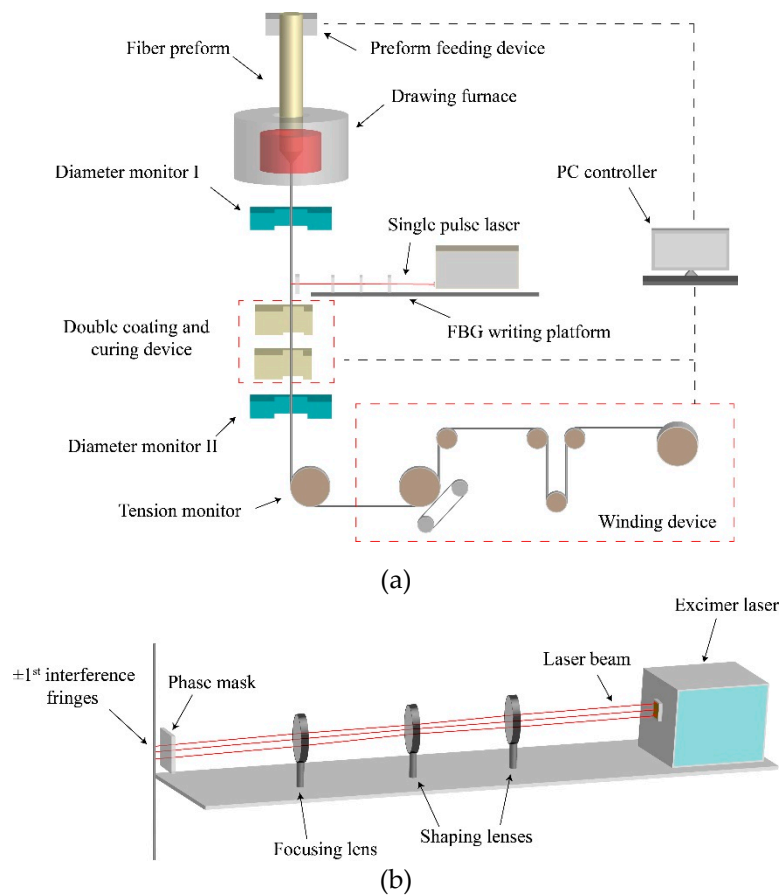


Figure 4. (a) Schematic diagram of the FBG online fabrication processes on our customized drawing tower. (b) Schematic diagram of the phase mask writing platform.

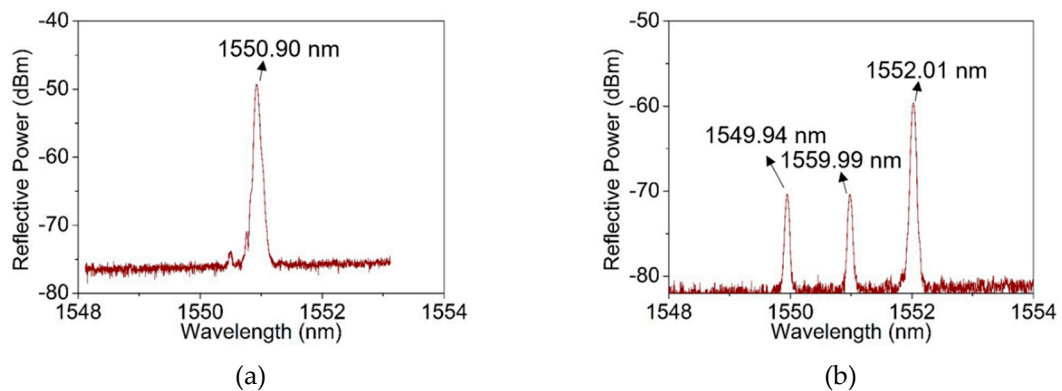


Figure 5. The experimental reflection spectrum of the FBG with the diameter of the fiber is (a) 125 μm and (b) 200 μm , the inset is the experimental optical field distribution.

4. Temperature and Curvature Sensing

The TM-FBG based fiber sensor was characterized for temperature and curvature sensing. The temperature experimental setup is shown in Figure 6. As seen from the figure, we selectively chose a fiber section with FBG inscription as the temperature unit. Figure 7a exhibits the red-shift of the center wavelength of three reflections in the TM-FBG, when the temperature increased from 30 $^{\circ}\text{C}$ to 100 $^{\circ}\text{C}$ with a step of 10 $^{\circ}\text{C}$. The central wavelengths of the reflections of the LP_{01} and LP_{11}

modes under different temperature are plotted in Figure 7b. The results showed that both the LP_{01} and the LP_{11} modes had a similar temperature response of $11.2 \text{ pm}/^\circ\text{C}$, owing to the same transmission medium (fiber core), which had the same thermo-optical and expansion coefficients of the two modes. Indeed, the temperature response of the two-mode fiber was very close to the value of temperature response in a single-mode FBG ($10.7 \text{ pm}/^\circ\text{C}$) [21].

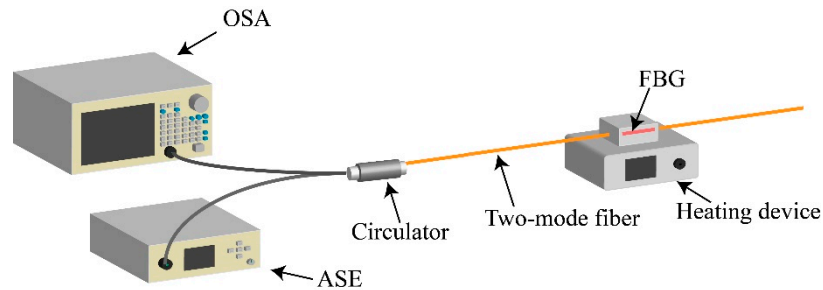


Figure 6. Schematic diagram of the two-mode FBG temperature experiment.

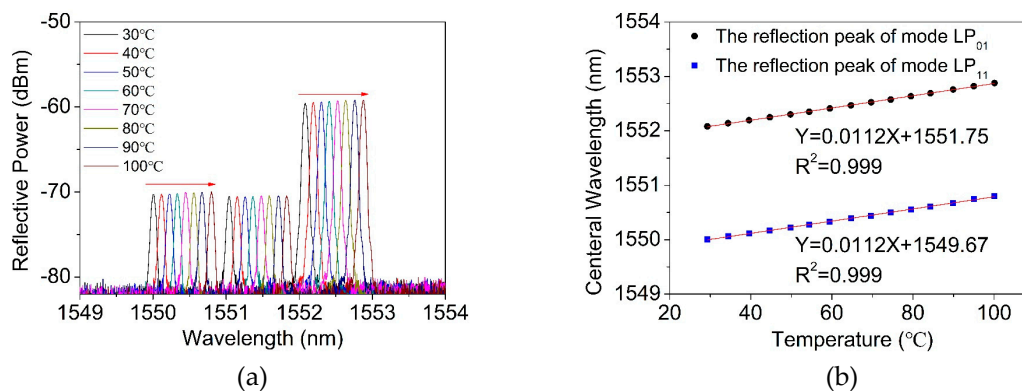


Figure 7. The experimental (a) reflection spectra and (b) wavelength shift of two-mode FBG with the temperature change.

The calculation in Figure 3 indicates that the mode confinement loss of the mode LP_{01} was much lower than that of the LP_{11} mode, when the fiber was bent. We then considered using the TM-FBG for bending measurements. An amplified spontaneous emission source (ASE, ASE-CL-20-B, WavePhotonics, Pittsfield, USA), an optical spectrum analyzer (OSA, AQ6370B, Yokogawa, Tokyo, Japan) and a circulator were used for the measurements. The experimental setup is depicted in Figure 8. The optical fiber was wrapped around a loop with an adjustable radius. The smaller the loop radius, the severer the bending applied to the TM fiber. As seen from the figure, we selectively chose a fiber section without FBG inscription as the bending unit, and this section was bent into a circle of different diameters. Figure 9a shows the reflection spectrum when the bending diameter changed from 67 mm to 26 mm. Figure 9b presents the reflected power as a function of the bending curvature, of the two modes. Only when the curvature was larger than 25 m^{-1} , the change of the transmission became obvious. From Figure 9b, when the curvature increased from 25 m^{-1} to 80 m^{-1} , the intensity of the reflection peak of the LP_{11} mode decreased at a rate of $-0.21 \text{ dB}/\text{m}^{-1}$, and the linearity was 0.991. On the contrary, the reflected peak intensity of the LP_{01} mode was almost kept unchanged at -60.932 dBm . Considering the actual intensity of the light source will fluctuate in the process, the variation of the reflection peak intensity of mode LP_{01} as the reference, it can modify the reflection peak results of mode LP_{11} , making the measurement of the fiber curvature more accurate. Figure 9c shows the difference change of reflectivity intensity between the two peaks with the increase of curvature. The near-field mode patterns were recorded using an infrared camera (Bobcat-320, Xenics) and plotted in Figure 9d. Clearly, we can observe that the LP_{11} mode was susceptible to the fiber bending, and therefore, led to a dimmed output.

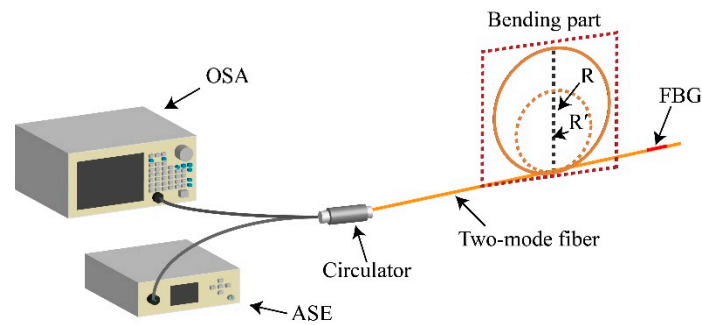


Figure 8. Schematic diagram of the two-mode FBG bending experiment.

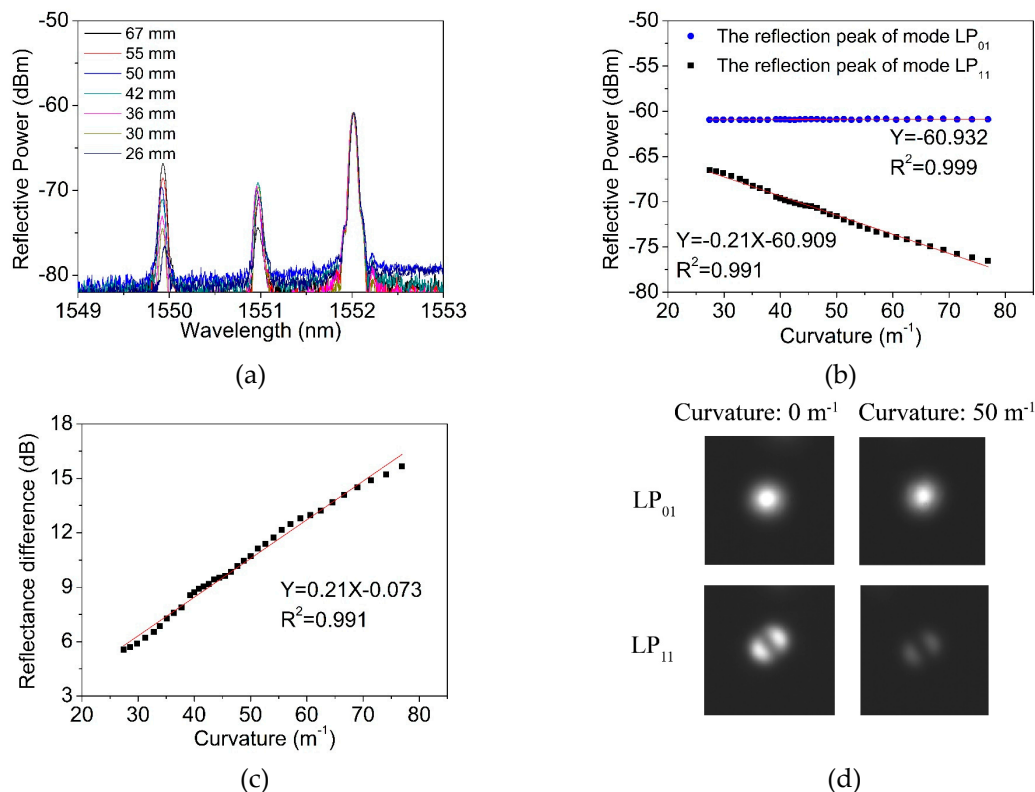


Figure 9. The experimental (a) reflection spectra, (b) peak intensity, (c) the difference of reflectivity intensity of two-mode FBG and (d) the transmission mode field with the curvature change.

5. TM-FBG Array and Its Application

Using the on-line FBG writing system on the drawing tower, a 100-meter-long two-mode FBG array with an equal grating spacing of 1 meter was inscribed. The total of the 100 FBGs were continuously written in a row without any splicing joint. The fabricated array was then demodulated using a grating interrogator (LGI-100B, Sentek Instrument, Blacksburg, VA, USA), using the wavelength scanning time division multiplexing (WSTDm) technique. This technique can accurately measure the central wavelength and reflection spectrum of each grating. Figure 10a,b show the spectra of 10 selected gratings located from 0 m to 100 m, with an interval of 10 m. Figure 10c plots the center wavelengths of each reflection peak in the FBG array, and the fluctuation was limited to less than 0.1 nm. Figure 10d shows the intensity of each reflection peak in the FBG array. The reflection peak intensity of mode LP_{01} was as high as around -40 dB, with a fluctuation of less than 5 dB: A similar level was found in a single-mode FBG array [22]. The intensity of the reflection peak of the LP_{11} mode was prone to external influences, and therefore, the fluctuation ramps up to ~ 8 dB. As seen in Figure 10d, the fluctuation of the coupled mode was unstable, with a value of ~ 16 dB. It is clear that the measurements with both

the LP₀₁ and LP₁₁ modes have good consistency and stability, making the TM-FBG array an effective sensing network for real applications.

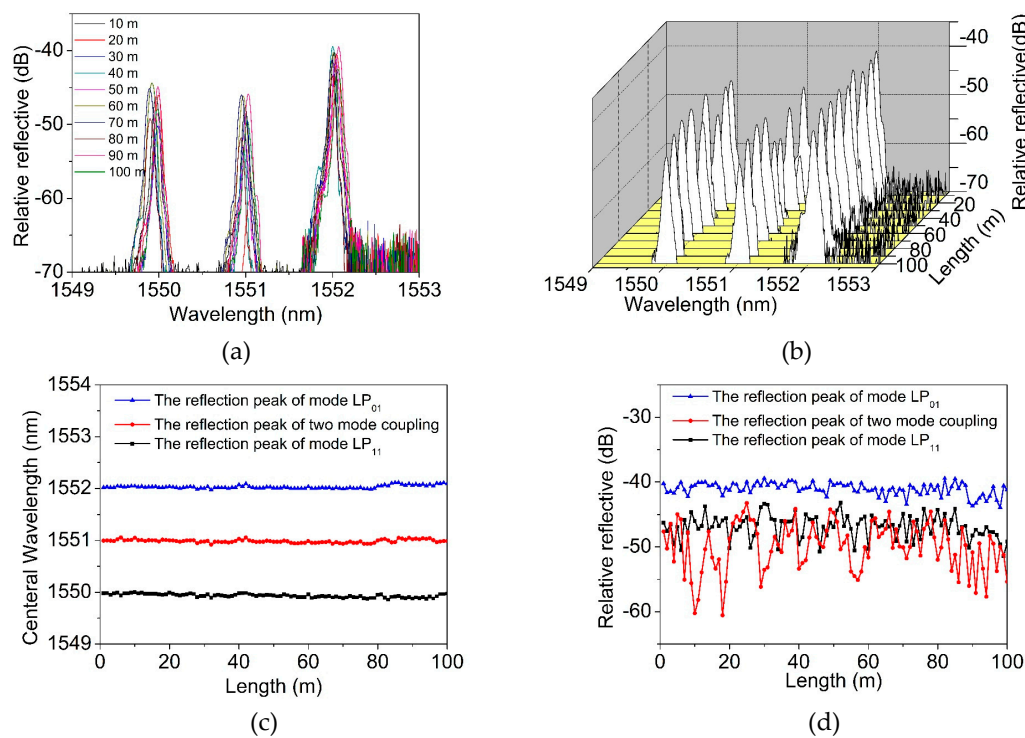


Figure 10. The measurements of two-mode FBG array for (a) and (b) spectra, (c) center wavelength, (d) reflection peak intensity.

The 100-meter-long TM-FBG array was further tested for quasi-distributed temperature sensing. The FBG array was placed into a chamber with temperature control, and the center wavelength of the LP₀₁ reflection was recorded. Figure 11a shows the variation of central wavelength when all FBGs were heated from 30 °C to 100 °C with a step of 10 °C. It can be seen that there was a slight red-shift. Figure 11b extracts the wavelength variation of the FBGs every 10 m, and we found that the wavelength shift and the change of temperature kept linear, as ~10.9 pm/°C.

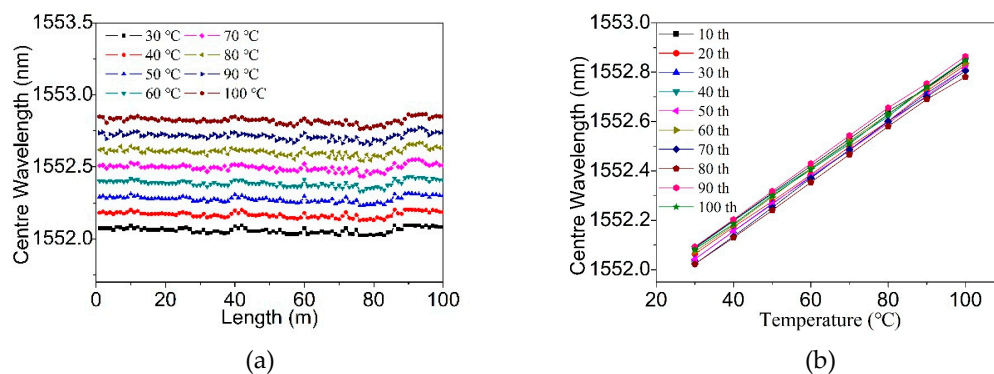


Figure 11. Variation of the center wavelength of (a) all FBGs and (b) selected FBGs when the temperature increase from 30 °C to 100 °C.

As discussed in Section 4, the reflected peak intensity of the LP₁₁ mode has a linear relationship with the curvature when it is larger than 25 m⁻¹ (corresponding to the bending diameter 80 mm). We then designed an experiment to verify the system for quasi-distributed curvature sensing. The setup is shown in Figure 12a. The FBG array was helically wound over a stick with a diameter of 50 mm.

The stick used for curvature sensing was made from polyethylene and propylene (PEP), which is the combination of polyethylene glycol (PEG) and propylene oxide (PO). The adjustable fixture clamped the wound part, applying pressure in this region. The influence of the fixture pressure is depicted in Figure 12b. When the pressure was applied, the sponge substrate was pressed and the curvature of the fiber increased rapidly towards the short axis, leading to a high bending loss. The vertex of the short axis had the maximum radius of curvature, with the bending radius defined as $R = a^2/b$ (a is the length of the long axis and b is the length of the short axis). The spatial resolution of this system can be adjusted by changing the winding density of fiber over the sponge substrate, and the sensitive threshold can be controlled by changing the diameter of the substrate material.

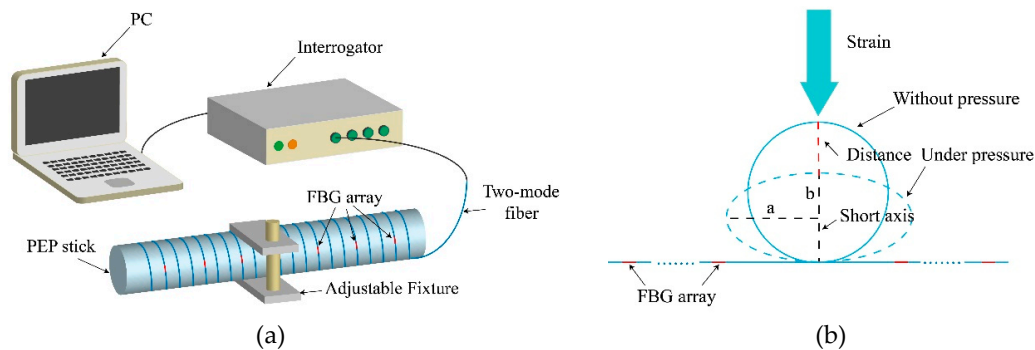


Figure 12. Schematic diagram of (a) the FBG array in the application of large curvature sensing; (b) the fiber is deformed by pressure.

Figure 13a shows the results of different bending degrees at a certain position. This position was chosen between the 4th and 5th FBG (corresponding to the area from 4 m to 5 m of the TM-FBG array). The bending degree of the fiber increased by reducing the length of the short axis. When the bending curvature increased, the intensity of the reflection peaks, located at 1 m, 2 m, 3 m and 4 m, were almost unchanged. However, from 5 m to the rest of the grating array, the measured reflection intensity significantly decreased with the increase of the deformation. It was therefore determined that the position of the deformation was located between 4 m and 5 m of the fiber. Figure 13b presents the reflection intensity of the FBGs at 4 m and 5 m when the deformation increased. It can be seen that the FBG at 4 m was hardly influenced, while the peak intensity of the FBG at 5 m was reduced. When the maximum curvature changed from 50 m^{-1} to 300 m^{-1} , the reflected peak intensity of the 5th FBG decreased at a rate of -0.056 dB/m^{-1} , and the linearity was 0.991. Note that in the measurements, the first few data points (marked with red circles in Figure 12b) failed to meet the expected trend. It was supposed that when the bending degree was low, errors could be large due to the tension raised during fiber winding.

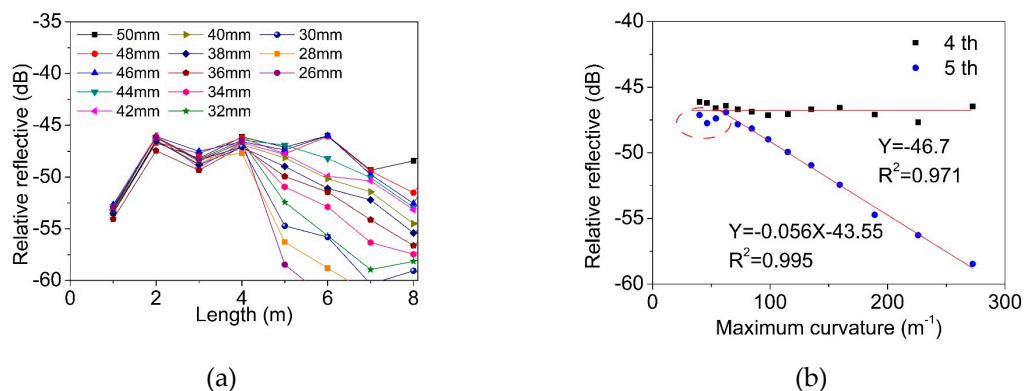


Figure 13. Relative change of reflection peak intensity for (a) all FBG and (b) single FBG when the axial strain distance from 0 mm to 24 mm.

As shown in Figure 14a, six positions were selected randomly and individual deformation was then applied. The measured results show that the first FBGs of the reflection peak intensity decreased were located at 5 m, 6 m, 10 m, 12 m, 16 m and 19 m. In general, this system can reliably identify the positions of the deformation spots. Moreover, to test the multi-position measurements, five positions were simultaneously applied the deformation at 10 mm, and the result is shown in Figure 14b. The deformation regions can be identified at 6 m to 7 m, 8 m to 9 m, 13 m to 14 m, 16 m to 17 m and 19 m to 20 m.

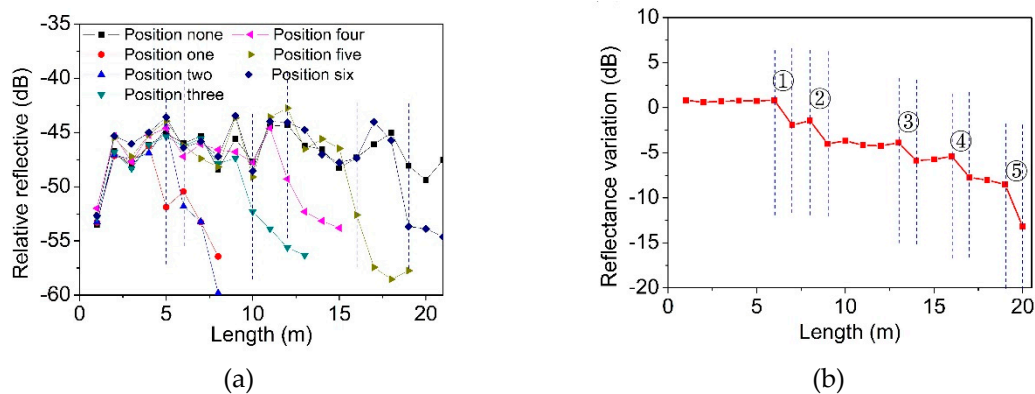


Figure 14. Variation of reflection peak intensity when the deformation is located in (a) a different area and (b) multiple areas.

The sensitivity of the temperature sensing was measured $\sim 10.9 \text{ pm}/^\circ\text{C}$ within the range from 30°C to 100°C . For the curvature sensing, the sensitivity reached $-0.056 \text{ dB}/\text{m}^{-1}$ in the range 50 m^{-1} to 300 m^{-1} . We used the central wavelength of the reflection peak of LP_{01} mode and LP_{11} mode to realize the temperature and measure curvature. Since the two physical modes were completely independent, therefore, dual-parameter measurement could be realized at the same time. Compared with an ordinary grating array, the current system could realize real-time temperature sensing, as well as a fast response to curvature changing. Such a system is suitable for being used as an alarm system to measure and locate one region with larger curvature, and monitor the temperature continuously.

6. Conclusions

In this paper, mode characteristics of a fiber with different diameters from $125 \mu\text{m}$ to $240 \mu\text{m}$ were theoretically investigated for the purpose of figuring out the conditions for two-mode fiber. The proposed fiber had a diameter of $200 \mu\text{m}$ and only two transverse modes (LP_{01} and LP_{11}) were supported. Using the on-line grating fabrication system, a TM-FBG array was successfully written and this TM-FBG array was further investigated for temperature and curvature sensing. The response to temperature was measured $11.2 \text{ pm}/^\circ\text{C}$ and the curvature response was $-0.21 \text{ dB}/\text{m}^{-1}$. Further, the TM-FBG array was analyzed using a grating interrogator. For quasi-distributed temperature sensing, the grating array performed similarly as a standard grating array, however, it possessed extensions for curvature measurements. The TM-FBG array could reliably determine the position and degree of bending along a structured object. It is believed, therefore, that such a system has potentials in many aspects regarding safety production or structural surveillance.

Author Contributions: Data curation, X.J. and H.G.; Funding acquisition, H.Y.; Methodology, H.Y., W.G., S.J. and Y.Z.; Supervision, H.Y.; Writing—original draft, W.G. and Y.Z.; Writing—review & editing, Y.Z.

Funding: This work was funded by the National Natural Science Foundation of China (NSFC) (Grant No. 61290311) and the Major Scientific and Technological Innovation Project in Hubei Province (Grant No. 2015AAA001).

Conflicts of Interest: The authors declare no conflict of interest.

References

1. Hill, K.O.; Meltz, G. Fiber Bragg Grating Technology Fundamentals and Overview. *J. Lightwave Technol.* **1997**, *15*, 1263–1276. [[CrossRef](#)]
2. Lee, B. Review of the present status of optical fiber sensors. *Opt. Fiber Technol.* **2003**, *9*, 57–79. [[CrossRef](#)]
3. Patrick, H.J.; Williams, G.M.; Kersey, A.D. Hybrid fiber Bragg grating/long period fiber grating sensor for strain/temperature discrimination. *IEEE Photonics Technol. Lett.* **1996**, *8*, 1223–1225. [[CrossRef](#)]
4. Araujo, F.M.; Ferreira, L.A.A. Simultaneous determination of curvature, plane of curvature, and temperature using a miniaturized sensing head based on fiber Bragg gratings. *Appl. Optics* **2002**, *41*, 2401–2407. [[CrossRef](#)]
5. Iadicco, A.; Cusano, A.; Cutolo, A. Thinned Fiber Bragg Gratings as High Sensitivity Refractive Index Sensor. *IEEE Photonics Technol. Lett.* **2004**, *16*, 1149–1151. [[CrossRef](#)]
6. Peng, P.C.; Tseng, H.Y.; Chi, S. Long-Distance FBG Sensor System Using a Linear-Cavity Fiber Raman Laser Scheme. *IEEE Photonics Technol. Lett.* **2004**, *16*, 575–577. [[CrossRef](#)]
7. Li, A.; Wang, Y.; Hu, Q.; Shieh, W. Few-mode fiber based optical sensors. *Opt. Express* **2015**, *23*, 1139–1150. [[CrossRef](#)]
8. Kim, B.Y.; Blake, J.N.; Huang, S.Y. Use of highly elliptical core fibers for two-mode fiber devices. *Opt. Lett.* **1987**, *12*, 729–731. [[CrossRef](#)]
9. Safaai-Jazi, A.; Mckeeman, J.C. Synthesis of intensity patterns in few-mode optical fibers. *J. Lightwave Technol.* **1991**, *9*, 1047–1052. [[CrossRef](#)]
10. Kumar, A.; Jindal, R.; Varshney, R.K. A Fiber-Optic Temperature Sensor Based on LP₀₁-LP₀₂ Mode Interference. *Opt. Fiber Technol.* **2000**, *6*, 83–90. [[CrossRef](#)]
11. Chen, J.; Lu, P.; Liu, D. Optical fiber curvature sensor based on few mode fiber. *Optik* **2014**, *125*, 4776–4778. [[CrossRef](#)]
12. Guan, B.O.; Tam, H.Y.; Tao, X.M. Simultaneous strain and temperature measurement using a superstructure fiber Bragg grating. *IEEE Photonics Technol. Lett.* **2000**, *12*, 675–677. [[CrossRef](#)]
13. Zhang, J.; Wan, H.; Zhang, L. All-fiber CW cylindrical vector beam fiber laser based on few-mode fiber Bragg grating. *Optik* **2017**, *147*, 109–114. [[CrossRef](#)]
14. Yuean, M.; Haisu, L.; Guobin, R. Vector mode conversion based on an asymmetric fiber Bragg grating in few-mode fibers. *Appl. Opt.* **2017**, *56*, 7305.
15. Yang, H.Z.; Ali, M.M.; Islam, M.R. Cladless few mode fiber grating sensor for simultaneous refractive index and temperature measurement. *Sens. Actuators A* **2015**, *228*, 62–68. [[CrossRef](#)]
16. Zheng, Y.; Yu, H.H.; Guo, H.Y. Analysis of the spectrum distortions of optical fiber Bragg gratings fabricated in-line on a draw tower by the phase mask technique. *J. Lightwave Technol.* **2014**, *33*, 2670–2673. [[CrossRef](#)]
17. Guo, H.Y.; Yu, H.H.; Wu, Y.W. Preparation of Photosensitive Fibers for Weak Fiber Bragg Grating Arrays. *Phys. Procedia* **2013**, *48*, 184–190. [[CrossRef](#)]
18. Snitzer, E. Cylindrical Dielectric Waveguide Modes. *J. Opt. Soc. Am.* **1961**, *51*, 491–498. [[CrossRef](#)]
19. Lu, S.; Xu, O.; Feng, S. Analysis of radiation-mode coupling in reflective and transmissive tilted fiber Bragg gratings. *J. Opt. Soc. Am.* **2009**, *26*, 91–98. [[CrossRef](#)]
20. Ademgil, H.; Haxha, S.; Gorman, T. Bending Effects on Highly Birefringent Photonic Crystal Fibers with Low Chromatic Dispersion and Low Confinement Losses. *J. Lightwave Technol.* **2009**, *27*, 559–567. [[CrossRef](#)]
21. Wang, Y.; Gong, J.; Dong, B. A Large Serial Time-Division Multiplexed Fiber Bragg Grating Sensor Network. *J. Lightwave Technol.* **2012**, *30*, 2751–2756. [[CrossRef](#)]
22. Guo, H.Y.; Tang, J.G.; Li, X.F. On-line writing identical and weak fiber Bragg grating arrays. *Chin. Opt. Lett.* **2013**, *11*, 030602.

